Stress-constrained Topology Optimization Using the Constrained Natural Element Method

Yanda Chen[1*], Eric Monteiro[1], Imade Koutiri[1] and Véronique Favier[1]

[1*]Laboratory PIMM, Arts et Metiers Institute of Technology, CNRS, CNAM, HESAM Universite, 151 Bd de l'Hôpital, 75013 Paris, France.

*Corresponding author(s). E-mail(s): yanda.chen@ensam.eu;
Contributing authors: eric.monteiro@ensam.eu;
imade.koutiri@ensam.eu; veronique.favier@ensam.eu;

Abstract

This paper presents a topology optimization framework to achieve volume minimization with Crossland fatigue constraints under proportional loading using the Constrained Natural Element Method. The local minimization problem is solved by means of the augmented Lagrangian method to deal with a large number of evaluation points. To suppress the numerical instabilities, a neighbor-based filter is proposed and compared to the widely used density filter. Furthermore, to circumvent the problem of stress singularity, several different relaxations of the constraints are also investigated. Compared with the topology optimization procedure based on the finite element method, the proposed method has the advantage of showing greater flexibility and convenience in discretization of complex design domains and the ability to maintain stable output under various discretization conditions.

Keywords: Topology optimization, Constrained Natural Element Method, Augmented Lagrangian method, Crossland fatigue criterion

1 Introduction

The history of structural optimization dates back to the early 20th century when Michell [1] derived formulas for the minimum weight arrangement of trusses. Then, Prager [2] and Rozvany [3] extended these principles and derived the topology optimization theory. Since Bendsøe and Kikuchi [4] proposed the homogenization method in their pioneering paper published in the late 1980s, this field has received extensive attention and various topology optimization methods have been proposed and applied to diverse physical problems. Currently, density-based methods and boundary variational methods have been widely used in topology optimization. The variants of the first class of methods include the solid isotropic material with penalization method (SIMP) (Ferrari and Sigmund [5]) and evolutionary procedures (Xia et al. [6]). The second class is represented by level set method (Lachouette et al. 2017) and phase field method (Wallin and Ristinmaa [7]). The comparison and critical review of the above classical methods have been given in detail by Sigmund and Maute [8].

Among the various topology optimization methods, density-based approaches are the best known, where the geometry is parameterized by a density function and the displacement field is usually solved by the finite element method (FEM). However, the most commonly used Lagrangian-type finite elements suffer from numerical instabilities such as checkerboard pathology and single-node connections (Diaz and Sigmund [9]). Although several studies have been conducted to prevent the occurrence of checkerboard, such as non-conforming elements (Jang et al. [10]), continuous approximations of material distribution (Matsui and Terada [11]), use of different discretization for design variables and analytical meshes (Paulino and Le [12]), etc., these schemes may lead to other forms of numerical instability like lack of convergence (Talischi et al [13]). A feasible alternative is to use polygonal finite elements to suppress checkerboard patterns and reduce mesh dependence (Talischi et al. [14]; Talischi et al. [15]). In addition to processing higher degree of geometric anisotropy, they offer additional advantages in terms of greater flexibility and better approximation accuracy (Talischi et al. [14]). Another way to alleviate the mesh sensitivity has been the usage of the boundary element method (BEM). In recent years, a series of models coupling the BEM with level set method for topology optimization have also been developed (Ullah and Trevelyan [16]; Oliveira and Leonel [17]; Simonetti et al. [18]).

As an alternative to FEM and BEM, meshless methods (MMs) enjoy the advantage in eliminating the labor-intensive process of constructing geometric meshes in the design domain. In practice, numerical simulation and design optimization within the design domain can be performed using only an arbitrarily scattered set of nodes, without extra efforts to maintain mesh connectivity. Several common MMs based on the global weak form (e.g. EFGM, RKPM) (Cho and Kwak [19]; Zhou and Zou [20]; Wang et al. [21]) and local weak form (e.g. MLPG) (Li and Atluri [22]) have been successfully applied to topology optimization of continuum structures. In addition to their use in combination with SIMP method in the aforementioned literature, they have also been

implemented with bi-directional evolutionary structural optimization (BESO) (Shobeiri, [23]) and level set (Luo et al. [24]; Neofytou et al. [25]) methods. The major drawback of these MMs is the way to impose the essential boundary conditions since the interpolation functions lack the Kronecker delta property. The main purpose of using the constrained natural element method (CNEM) in this study is to avoid the mesh dependency associated with the FEM and the limitations of the MMs mentioned previously.

Conventional topology optimization designs with minimum compliance aim to find the stiffest structure for a given volume constraint, regardless of the material strength limitations. As a result, manual adjustments or shape optimization is required to enable the structure to withstand the applied loads. To ensure that structural components are produced to meet specific functional requirements, structural failure must be prevented at every point of the component, for example, by developing specific topology optimization schemes that allow the design to meet a given stress-based requirement and even maintain the fatigue life during a given number of load cycles. The main issues encountered in stress-based topology optimization are the singularity phenomenon (Rozvany [26]) and the large-scale optimization problem caused by the local behavior of constraints (Duysinx and Bendsøe [27]). Since the Crossland fatigue criterion under consideration is based on stress invariants, the fatigue-driven problem has the same difficulties as mentioned above.

Several techniques have been developed to solve topology optimization problems with stress constraints. In general, the singular optima is solved through relaxation techniques such as the ε-relaxation (Cheng and Guo [28]; París et al. [29]) or the qp-method (Bruggi [30]). Their basic idea is to expand the design space while making the intermediate density produce very high stress. Due to the local nature of stress constraints, constraint aggregation techniques are widely used to deal with a large number of constraints. The strategy of constraint aggregation is to construct the global stress measure for the whole design domain or for each subdomain by using a smoothed approximation of the maximum function, such as the Kreisselmeier –Steinhauser function (Kreisselmeier and Steinhauser [31]; París et al. [29]), the P-mean function (Duysinx and Sigmund [27]) and P-norm function (Duysinx and Sigmund [27]; Le et al. [32]; Lee et al. [33]; Fan et al. [34]). The global constraint function reduces the computational cost at the expense of losing control over the local behavior, and the quality of which depends on the number of aggregated constraints and the parameters used in the aggregation technique. As a result, the solution to the global problem can be different from the solution to the local one. Although increasing the number of subdomains leads to increased control of local stresses, there is no clear relationship between the number of subdomains and the quality of results (Le et al. [32]). Alternative techniques have been proposed in the literature to improve the accuracy of the aggregation, such as the improved aggregation by Kennedy and Hicken [35] or using the maximum rectifier function in Norato et al. [36]. However,

the above techniques are still parameter dependent and may not strictly satisfy the stress constraints. Recently, the augmented Lagrangian (AL) method has been shown to significantly reduce the cost associated with a large number of constraints while providing a more consistent model than aggregation techniques. For example, da Silva et al. [37, 38] applied the AL approach to deal with the uniform manufacturing uncertainties and compliant mechanism design in stress-constrained topology optimization without using aggregation techniques. Giraldo-Londoño and Paulino [39] developed a Matlab implementation of stress-constrained topology optimization using the polygonal finite element method and a scheme based on the AL method.

Materials and components used in critical load-bearing applications are usually subjected to cyclic loading, it is necessary to take multi-axial fatigue damage into account in topology optimization due to the multi-axial nature of the stresses. In order to enable the addition of fatigue failure constraints, several static and quasi-static fatigue models have been developed for topology optimization of linear elastic structures, thereby avoiding the high computational cost when facing a large number of loading sequences. Sherif et al. [40] addressed the dynamic property of load conditions in topology optimization by applying equivalent static loads. Holmberg et al. [41] imposed stress constraints instead of fatigue constraints in topology optimization. Jeong et al. [42] developed the topology optimization method with dynamic fatigue and static failure constraints under proportional loads. Collet et al. [43] proposed an optimization tool for lightweight design accompanied by compliance and fatigue constraints through a modified Goodman failure criterion based on Sines theory. Using the Palmgren-Miner's linear damage rule, S-N curves and Sines fatigue criterion, Oest and Lund [44] investigated topology optimization under finite-life fatigue constraints. Chen et al. [45] considered the fatigue constrained topology optimization with cumulative fatigue damage and discussed the influence of damage penalization parameters and load parameters on the final design. The above topology optimization studies assumed a single loading mode. In addition, a series of studies have been conducted to solve the topology optimization problem under multiple and complex loads. James and Waisman [46] considered structural topology optimization for multiple load cases and explored a damage superposition method to calculate the individual damage fields induced by each individual load case. Zhang et al. [47] predicted the fatigue life of non-proportional loading by using the signed von Mises stress. Suresh et al. [48] used a continuous time approach in topology optimization to handle general load histories that include non-proportional loading. Subsequently, this model was extended to the fatigue-constrained topology optimization for materials with transversely isotropic properties [49]. The similarities of the above studies lie in the use of FEM to solve the equilibrium equation and employ aggregation technology or active set strategy to reduce the number of constraints.

This paper extends the augmented Lagrangian method applied in *PolyStress* (Giraldo-Londoño and Paulino [39]) to topology optimization

problems with fatigue constraints, and also compares the performance of the two procedures in solving topology optimization with von Mises stress constraints. The reminder of this paper is organized as follows. Section 2 discusses the use of CNEM to solve partial differential equations (PDEs) in topology optimization problems. Section 3 presents the topology optimization problems with fatigue constraints for continuum structures, and Section 4 describes the implementation of the optimizer and compares the behavior of different constraint relaxations with a two-dimensional simple example. Then, several numerical examples are shown in Section 5. Finally, Section 6 gives concluding remarks to complete the paper. The procedure of sensitivity analysis for stress and fatigue constrained topology optimization problems are given in Appendices A and B, respectively.

2 Mechanical formulation

2.1 Constrained natural element method

The CNEM is a halfway between MMs and FEM, enjoying the advantages of both. In CNEM, the constrained Voronoi diagram of a cloud of N nodes divides the bounded domain Ω^D in D-dimensions into a group of Voronoi cells $\mathcal{V}_i$ conformed to domain boundaries, as shown in Fig. 1, such that any point x within the Voronoi cell $\mathcal{V}_i$ is closer to node i than any other node $j (j \neq i)$ (Yvonnet et al. [50]).

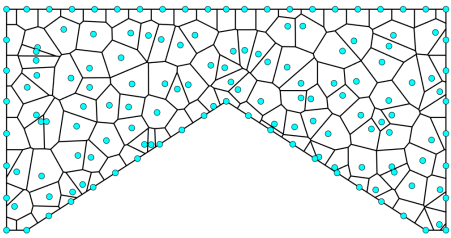

Fig. 1 Constrained Voronoi diagram of a cloud of N nodes in 2D

The CNEM uses the natural neighbor-based interpolation schemes such as the Sibson interpolation (Sibson [51]) and the Laplace interpolation (Belikov and Belikov [52]). The former one is applied in this paper and the construction of which in 2D is shown in Fig. 2. First, the original Voronoi diagram is locally modified by introducing a new Voronoi cell attached to point $\boldsymbol{x}$ (blue area). Then, the interpolation function is computed from geometrical considerations:

$$\phi_i(\boldsymbol{x}) = \frac{V_i(\boldsymbol{x})}{V(\boldsymbol{x})} \text{ with } V(\boldsymbol{x}) = \sum_{i=1}^{n} V_i(\boldsymbol{x}) \tag{1}$$

where $V_i(\boldsymbol{x})$ is the area of the intersection (green area) of Voronoi cell attached to a neighbor a (yellow area) and the new Voronoi cell (blue area), $V(\boldsymbol{x})$ represents the area of the new Voronoi cell.

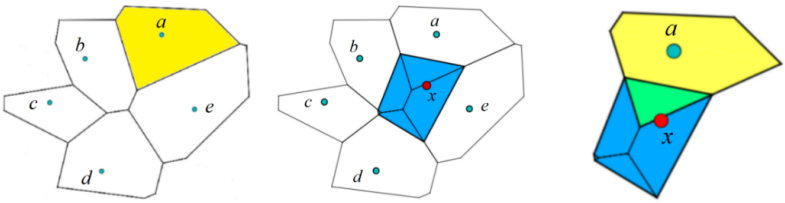

Fig. 2 Process to compute Sibson interpolant in 2D

The Sibson interpolation function enjoys several properties such as the Kronecker delta property, partition of unity and linear consistency (Sukumar et al. [53]). However, the interpolation functions are non-polynomial in nature. To perform numerical integration, the stabilized conforming nodal integration scheme (Chen et al.[54]) is used in this paper. For futher details on CNEM, the reader can refer to Yvonnet et al. [50].

2.2 Linear elastic partial differential equations

This research focuses on the topology optimization problem with high cycle fatigue criteria constraints. High cycle fatigue refers to a kind of fatigue caused by small elastic strain under a large number of load cycles before failure occurs. Therefore, the type of PDEs considered here is linear elastic. In addition, the material is homogeneous and isotropic. The equilibrium equation is expressed as follows:

$$\begin{cases} \bigtriangledown \boldsymbol{\sigma} + \boldsymbol{b} = \boldsymbol{0} & \text{in } \Omega \\ \boldsymbol{\sigma n} = \bar{\boldsymbol{t}} & \text{on } \Gamma_t \\ \boldsymbol{u} = \overline{\boldsymbol{u}} & \text{on } \Gamma_u \end{cases} \tag{2}$$

where $\boldsymbol{\sigma}$ is the symmetric Cauchy stress tensor, $\boldsymbol{b}$ is the body force vector, $\overline{\boldsymbol{u}}$ and $\bar{\boldsymbol{t}}$ are prescribed displacement vector and traction vector respectively, Γ_t and Γ_d represent homogeneous Dirichlet boundary and Von Neumann boundary respectively, $\boldsymbol{n}$ is the outer normal unit vector at the boundary $\Gamma = \Gamma_t \cup \Gamma_u$.

The weak form of Eq. 2 can be obtained by introducing a trial function $\boldsymbol{\delta u}(\boldsymbol{x}) \in \boldsymbol{H}^1$, where $\boldsymbol{H}^1$ is the Sobolev space, and carried out integration over the domain:

$$\int_\Omega \boldsymbol{\delta \varepsilon}^T \boldsymbol{\sigma} \, d\Omega - \int_\Omega \boldsymbol{\delta u}^T \boldsymbol{b} \, d\Omega - \int_{\Gamma_t} \boldsymbol{\delta u}^{\boldsymbol{T}} \, \bar{\boldsymbol{t}} \, d\Gamma = 0 \tag{3}$$

In order to solve the weak form numerically, the geometric domain needs to be discretized. The displacement is then approximated by $\boldsymbol{u}^h(\boldsymbol{x})$:

$$\boldsymbol{u}^h(\boldsymbol{x}) = \sum_{i=1}^{N} \boldsymbol{\Phi}_i(\boldsymbol{x})\boldsymbol{u}_i \tag{4}$$

where $\boldsymbol{\Phi}_i$ and $\boldsymbol{u}_i$ are the interpolation function matrix and displacement vector of node i respectively. The strain vector $\boldsymbol{\varepsilon}^h$ at position $\boldsymbol{x}$ becomes:

$$\boldsymbol{\varepsilon}^h(\boldsymbol{x}) = \boldsymbol{L}\boldsymbol{u}^h(\boldsymbol{x}) = \sum_{i=1}^{N} \boldsymbol{B}_i(\boldsymbol{x})\boldsymbol{u}_i \tag{5}$$

where $\boldsymbol{L}$ is the differential operator matrix, $\boldsymbol{B}_i$ represents the strain-displacement matrix of node i. Finally, the stress vector $\boldsymbol{\sigma}^h$ can be obtained by using the constitutive equation:

$$\boldsymbol{\sigma}^h(\boldsymbol{x}) = \sum_{i=1}^{N} \boldsymbol{C}\boldsymbol{B}_i(\boldsymbol{x})\boldsymbol{u}_i \tag{6}$$

where $\boldsymbol{C}$ is the material constitutive matrix. Substituting Eqs. 4, 5 and 6 into Eq. 3, the discrete weak form becomes:

$$\sum_{j=1}^{N}\sum_{i=1}^{N} \boldsymbol{\delta u}_j^T \left(\int_{\Omega} \boldsymbol{B}_j^T \boldsymbol{C}\boldsymbol{B}_i d\Omega \right) \boldsymbol{u}_i = \sum_{j=1}^{N} \boldsymbol{\delta u}_j^T \left(\int_{\Gamma_t} \boldsymbol{\Phi}_j^T \, \bar{\boldsymbol{t}} \, d\Gamma + \int_{\Omega} \boldsymbol{\Phi}_j^T \, \boldsymbol{b} \, d\Omega \right) \tag{7}$$

Using the arbitrariness of $\boldsymbol{\delta u}$, Eq. 7 yields to the following matrix system:

$$\boldsymbol{K}\boldsymbol{u} = \boldsymbol{f} \tag{8}$$

where $\boldsymbol{K}$ and $\boldsymbol{f}$ represent the global stiffness matrix and the load vector respectively.

3 Topology optimization formulation

In this section, the topology optimization formulation with local fatigue constraints for continuum structures using the density-based method is presented. The general optimization statement in this study can be expressed mathematically as follows:

$$\begin{aligned} \min\ & f(\boldsymbol{\rho}) = \sum_{i=1}^{N} \rho_i V_i \\ \text{s.t.}\ & \begin{cases} g_i(\boldsymbol{\rho}, \boldsymbol{u}) \leq 0, & i = 1, \dots N \\ 0 \leq \rho_j \leq 1, & j = 1, \dots N \end{cases} \\ \text{with:}\ & \boldsymbol{K}(\boldsymbol{\rho})\boldsymbol{u} = \boldsymbol{f} \end{aligned} \tag{9}$$

where f is the objective function, $\boldsymbol{\rho}$ is the vector of design variables, g_i is the i-th fatigue constraint, which depends not only on the design variables, but also on the displacement.

3.1 Density-based method

The direct use of design variable $\boldsymbol{\rho}$ to solve Eq. 9 does not make it a well-posed problem. In this study, the polynomial filter used by Zegard and Paulino [55] is adopted, such that $\widetilde{\boldsymbol{\rho}} = \boldsymbol{\mathcal{F}}\boldsymbol{\rho}$:

$$\mathcal{F}_{ij} = \frac{H_{ij}^{den}\rho_j}{\sum_{k=1}^{N} H_{ik}^{den}\rho_k}, \text{ with } H_{ij}^{den} = \max\left[0, 1 - \frac{d\left(\boldsymbol{x}_i, \boldsymbol{x}_j\right)}{R}\right]^s \tag{10}$$

where R is the radius of the filter and $s \geq 1$ the exponent. The polynomial filter reduces to a conventional linear filter when $s = 1$. Note that large values of s (e.g. $s \geq 5$) may cause small branches to appear due to low contribution of distant elements. Fig. 3 shows the linear and polynomial filters for a regular node distribution. The advantage of using a polynomial instead of a linear function is that it reduces the influence of more distant elements and facilitates more abrupt changes in density, thereby better defining the geometry boundaries.

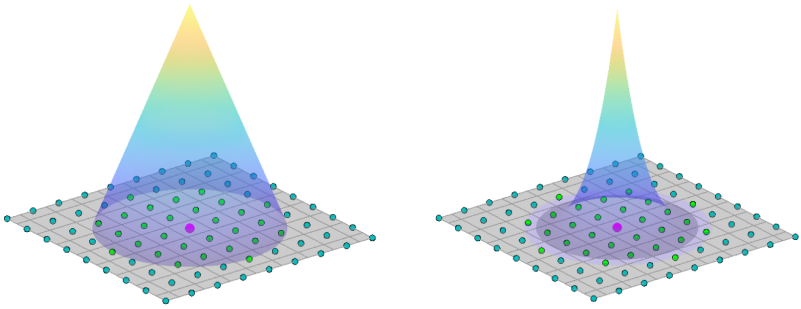

Fig. 3 Linear filter $s = 1$ (left) and polynomial filter $s = 3.5$ (right) in 2D

To enhance the filtering effect when the design domain or the distribution of nodes is irregular, a neighbor-based filter is proposed which can more reasonably consider the contribution of neighbor nodes in all directions and the only parameter that needs to be defined is the number of layers. For example, the density of node i in Fig. 4 is mainly contributed by the nodes on the left and bottom, while the nodes on the right do not even contribute to it. The neighbor-based filter can reasonably take into account the uneven spatial distribution of nodes. When the filtering area is determined, both of them are convolution based on the maximum distance from node in filtering region to the target node. The weight factor H_{ij} for neighbor-based filter can be rewritten as:

$$H_{ij}^{nei} = \begin{cases} \max\left[0, 1 - \frac{d(\boldsymbol{x}_i, \boldsymbol{x}_j)}{d_{max}}\right]^s & \text{if } j \text{ is a neighbor of } i \\ 0 & \text{else} \end{cases} \tag{11}$$

where d_{max} is the maximum distance between the target node (pink node) and its neighbors within the filtering domain (green nodes).

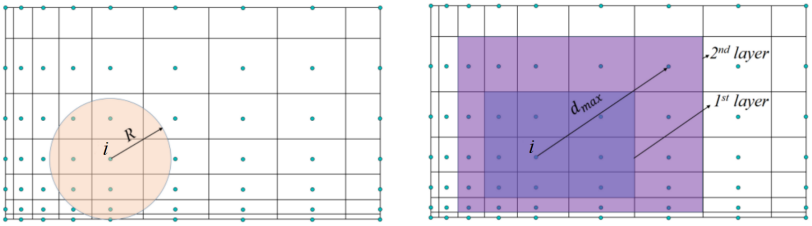

Fig. 4 Filter domain of density filter (left) and neighbor-based filter (right) under irregular situation

To obtain a black-and-white design without numerical instability, the so-called three field approach (Sigmund and Maute [8]) is adopted, which operates with the design variable $\boldsymbol{\rho}$, the filtered field $\widetilde{\boldsymbol{\rho}}$ and the projected field $\bar{\boldsymbol{\rho}}$. The Heaviside projection function used in this study is expressed as follows (Guest et al. [56]; Wang et al. [57]):

$$\bar{\rho}_i = \frac{\tanh(\beta\eta) + \tanh\left[\beta\left(\tilde{\rho}_i - \eta\right)\right]}{\tanh(\beta\eta) + \tanh[\beta(1-\eta)]} \tag{12}$$

where η is the projection threshold, β controls the slope of the function near the threshold parameter η.

Finally, the stiffness matrix $\boldsymbol{K}$ in Eq. 9 is calculated through a typical assembly process:

$$\boldsymbol{K}(\overline{\boldsymbol{\rho}}) = \sum_{i=1}^{N} \mathbb{A}^i \boldsymbol{K}_i, \text{ with } \boldsymbol{K}_i = \left[\epsilon + (1-\epsilon)\bar{\rho}_i^p\right] \boldsymbol{K}_{i0} \tag{13}$$

where $\boldsymbol{K}_i$ is the stiffness matrix of Voronoi cell i, $\mathbb{A}$ is an assembly operator, ϵ is the Ersatz parameter to prevent singularity, p is the penalty factor, $\boldsymbol{K}_{i0}$ is the stiffness matrix of Voronoi cell i when $\bar{\rho}_i = 1$.

3.2 Crossland fatigue criterion constraint

In order to obtain the optimal design that will not fail under the high cycle fatigue loading, it is important to consider high cycle fatigue criteria during the optimization. Among the current stress-based multi-axial fatigue criteria, the Crossland criterion (Crossland [58]) is attractive for the engineering design of high-performance components due to its ease of use, and it is expressed as follows:

$$g_i(\overline{\boldsymbol{\rho}}, \boldsymbol{u}) = \frac{1}{\beta_c}\sqrt{J_{2,a}^i} + \frac{\alpha_c}{\beta_c}\sigma_{H,max}^i - 1 \leq 0 \tag{14}$$

where $J_{2,a}^i$ and $\sigma_{H,\,\max}^i$ stand for the amplitude of the second stress invariant and the maximum value of hydrostatic stress for node i during the cyclic loading time T:

$$\begin{cases} J_{2,a}^i = \left(\boldsymbol{\sigma}_a^i\right)^T \boldsymbol{M}_c \boldsymbol{\sigma}_a^i \\ \sigma_{H,max}^i = \max\limits_{0\leq t\leq T}\left[\frac{\left(\sigma_{xx}^i+\sigma_{yy}^i+\sigma_{zz}^i\right)(t)}{3}\right] \end{cases} \tag{15}$$

where $\boldsymbol{\sigma}_a^i$ is the amplitude of Cauchy stress vector of node i: ,

$$\boldsymbol{\sigma}_a^i = \left[\max_{0\leq t\leq T}\boldsymbol{\sigma}^i(t) - \min_{0\leq t\leq T}\boldsymbol{\sigma}^i(t)\right]/2 \tag{16}$$

and

$$\boldsymbol{M}_c = \begin{bmatrix} 1/3 & -1/6 & 0 \\ -1/6 & 1/3 & 0 \\ 0 & 0 & 1 \end{bmatrix} \tag{17}$$

when plane stress is considered in 2D calculation.

The load applied in this paper is a constant amplitude cyclic load with the stress ratio $\sigma_{min}/\sigma_{max} = -1$. According to the definition of Crossland

criterion, the effect of load frequency on fatigue life can be neglected and the fatigue damage during one cyclic and a large number of cycles (i.e. $10e5$) are consistent in calculation. Therefore, the fatigue critera is evaluated only for one load cycle. The parameters α_c and β_c in Eq. 14 are material parameters: $\alpha_c = 3t_{-1}/f_{-1} - \sqrt{3}$, $\beta_c = t_{-1}$, where t_{-1} represents the fully reversed torsion fatigue limit, f_{-1} is the fagitue limit under fully reversed bending.

The Crossland fatigue criterion reduces to von Mises stress criterion in static loading with $\alpha_c = 0$ and $\beta_c = \bar{\sigma}/\sqrt{3}$ in which $\bar{\sigma}$ stands for the yield stress. In this case, the von Mises stress σ^i_{vm} associated with node i is given by

$$\sigma^i_{vm} = \sqrt{(\boldsymbol{\sigma}^i)^T \boldsymbol{M} \boldsymbol{\sigma}^i} \tag{18}$$

where $\boldsymbol{\sigma}^i = \begin{bmatrix} \sigma_{xx} & \sigma_{yy} & \tau_{xy} \end{bmatrix}^T$ is the vector of Cauchy stress at node i and $\boldsymbol{M} = 3\boldsymbol{M}_c$.

4 Augmented Lagrangian method

The method of moving asymptotes (MMA) is widely used in topology optimization applications. However, this optimizer is suitable for a large number of design variables and a small number of constraints. When a large number of local constraints are involved, it is common to use aggregation techniques to convert local constraints into global ones so that the computational time can be reduced (Bruggi [30]). Unfortunately, this approach introduces new difficulties, e.g. aggregation functions often do not give an accurate approximation of the maximum local function value. The reason is that the choice of aggregation function is often a compromise between two conflicting requirements: (1) to accurately approximate the maximum local function value and (2) to be smooth enough to prevent numerical instability when solving the problem using gradient-based optimizer.

An attractive alternative dealing with local constraints is the AL method. This technique converts the original constrained optimization problem in Eq. 9 into an unconstrained one by adding the constraints to the objective function in the form of penalization terms as described in details in Bertsekas [59]. To solve the new unconstrained problem, an iterative scheme is generally used in which the new objective function, at iteration k, is expressed as follows:

$$\min \; J^{(k)}(\overline{\boldsymbol{\rho}}, \boldsymbol{\lambda}, \mu) = f(\overline{\boldsymbol{\rho}}) + \frac{1}{N} \sum_{j=1}^{N} \left[\lambda_j^{(k)} h_j(\overline{\boldsymbol{\rho}}, \boldsymbol{u}) + \frac{\mu^{(k)}}{2} h_j(\overline{\boldsymbol{\rho}}, \boldsymbol{u})^2 \right] \tag{19}$$

where

$$h_j(\overline{\boldsymbol{\rho}}, \boldsymbol{u}) = \max\left[g_j(\overline{\boldsymbol{\rho}}, \boldsymbol{u}), -\frac{\lambda_j^{(k)}}{\mu^{(k)}}\right] \tag{20}$$

are equality constraints, $\lambda_j^{(k)}$ is the Lagrange multiplier estimator and $\mu^{(k)} > 0$ is a penalty coefficient. $\lambda_j^{(k)}$ and $\mu^{(k)}$ are updated at each iteration as follows (Senhora et al. [60]):

$$\begin{aligned} \mu^{(k+1)} &= \min\left[\alpha\mu^{(k)}, \mu_{max}\right] \\ \lambda_j^{(k+1)} &= \lambda_j^{(k)} + \mu^{(k)} h_j\left(\overline{\boldsymbol{\rho}}^{(k)}, \boldsymbol{u}\right) \end{aligned} \tag{21}$$

where $\alpha > 1$ is a constant parameter and μ_{max} is the upper limit which is used to prevent numerical instabilities. According to Giraldo-Londoño and Paulino [39], the value of α should be small so that $\mu^{(k)}$ grows at a moderate speed between successive AL subproblems. Large values may lead to ill-conditioning issues. In each AL iteration, the minimization of the AL function in Eq. 19 is replaced by a series of minimization of approximate convex sub-problems using MMA. The algorithm stops when the maximum change of the design variables between two successive iterations is lower than a given tolerance δ and all constraints are satisfied within another tolerance δ_s. In case of non convergent solution, a maximum number of iterations $MaxIter$ is defined arbitrarily. The schematic flowchart of the AL-based topology optimization framework is shown in Fig. 5. For details on the construction of the convex approximation function and the updating of the design variables, please refer to Giraldo-Londoño and Paulino [39].

4.1 Simple example

In this subsection, the density-based approach is investigated by introducing a simple example and analyze the effect of different relaxation forms of the constraints on the optimization results. Fig. 6(a) shows the geometry and boundary conditions of the example. The model consists of a square of length $L = 3$, divided into 3×3 Voronoi cells. The density of the cells is fixed to 1 except for two edge elements whose densities are controlled by the design variables ρ_1 and ρ_2. The topology optimization of this example with von Mises stress and Crossland fatigue constraints are analyzed. However, since both constraints give similar results, only the results involving von Mises stress constraints are shown here. The optimization statement is formulated as follows:

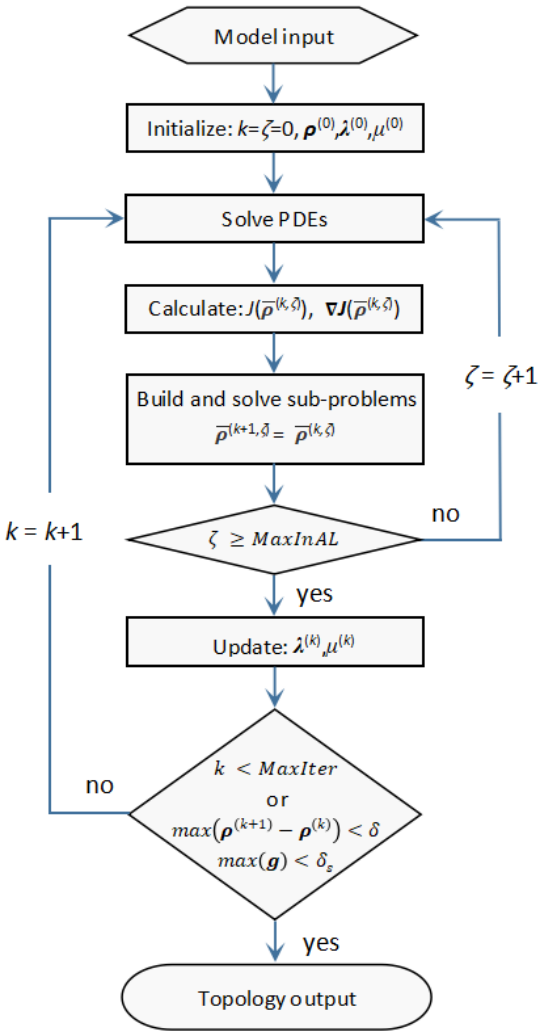

Fig. 5 Schematic flow chart of topology optimization framework based on AL

$$
\begin{aligned}
&\min\ f(\overline{\boldsymbol{\rho}}) = \frac{1}{|\Omega|}\sum_{i=1}^{N}\overline{\rho}_i V_i \\
&\text{s.t.}\begin{cases} g_i(\overline{\boldsymbol{\rho}}, \boldsymbol{u}) = \frac{\sigma_i^{VM}}{\bar{\sigma}} - 1 \leq 0, & i = 1,2 \\ 0 \leq \rho_j \leq 1, & j = 1,2 \end{cases} \\
&\text{with:} \qquad \boldsymbol{K}(\overline{\boldsymbol{\rho}})\boldsymbol{u} = \boldsymbol{f}
\end{aligned}
\tag{22}
$$

where $|\Omega|$ is the volume of the entire design domain and the yield stress $\bar{\sigma} = 1.1$. The Young's modulus and Poisson's ratio are $E_0 = 1$ and $\mu = 0.3$, respectively. The load is $\boldsymbol{f} = [0.12\,;\ -0.12]$, applied at the top right corner. No filter or projection is used in this problem, hence $\overline{\boldsymbol{\rho}} = \widetilde{\boldsymbol{\rho}} = \boldsymbol{\rho}$.

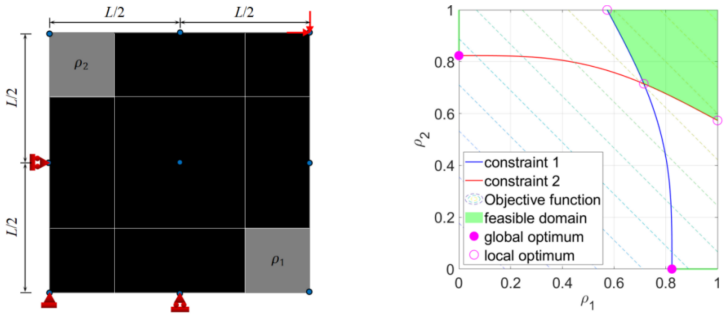

Fig. 6 Simple example: (a) geometry and boundary conditions and (b) feasible domain

4.2 Piecewise vanishing constraint solved by augmented Lagrangian method

In the AL-based formula, the constraint term no longer exists and the volume minimization problem under stress constraints is transformed into solving the approximate convex sub-problems in each step and moving towards the direction where the function J has no increasing value. Fig. 7 gives the J functions for the simple example with different constraint relaxations at the initial point, in which $\boldsymbol{\lambda}^{(0)} = \mathbf{0}$ and $\mu^{(0)} = 10$:

$$qp \text{ - relaxation: } \widetilde{g}_i(\overline{\boldsymbol{\rho}}) = \frac{\overline{\rho}_i^{p-q}\sigma_i^{VM}}{\bar{\sigma}} - 1 \tag{23a}$$

$$\text{Vanishing constraint: } \widetilde{g}_i(\overline{\boldsymbol{\rho}}) = \overline{\rho}_i g_i \tag{23b}$$

$$\text{SIMP-type linear constraint: } \widetilde{g}_i(\overline{\boldsymbol{\rho}}) = [\epsilon + (1-\epsilon)\overline{\rho}_i^p]\, g_i \tag{23c}$$

$$\text{SIMP-type cubic constraint: } \widetilde{g}_i(\overline{\boldsymbol{\rho}}) = [\epsilon + (1-\epsilon)\overline{\rho}_i^p]\, g_i^3 \tag{23d}$$

$$\text{Polynomial vanishing constraint: } \widetilde{g}_i(\overline{\boldsymbol{\rho}}) = [\epsilon + (1-\epsilon)\overline{\rho}_i^p]\, g_i \left(g_i^2 + 1\right) \tag{23e}$$

It can be noticed that hills appear in low density regions (yellow parts) in the first two forms in Fig. 7(a) and Fig. 7(b), which may cause the algorithm to fail to go downhill. On the contrary, when a SIMP-like relaxation is applied to the constraint, the convergence is faster and the objective function decreases to a minimum easily, as shown in Fig. 7(c). The cubic SIMP-type constraint

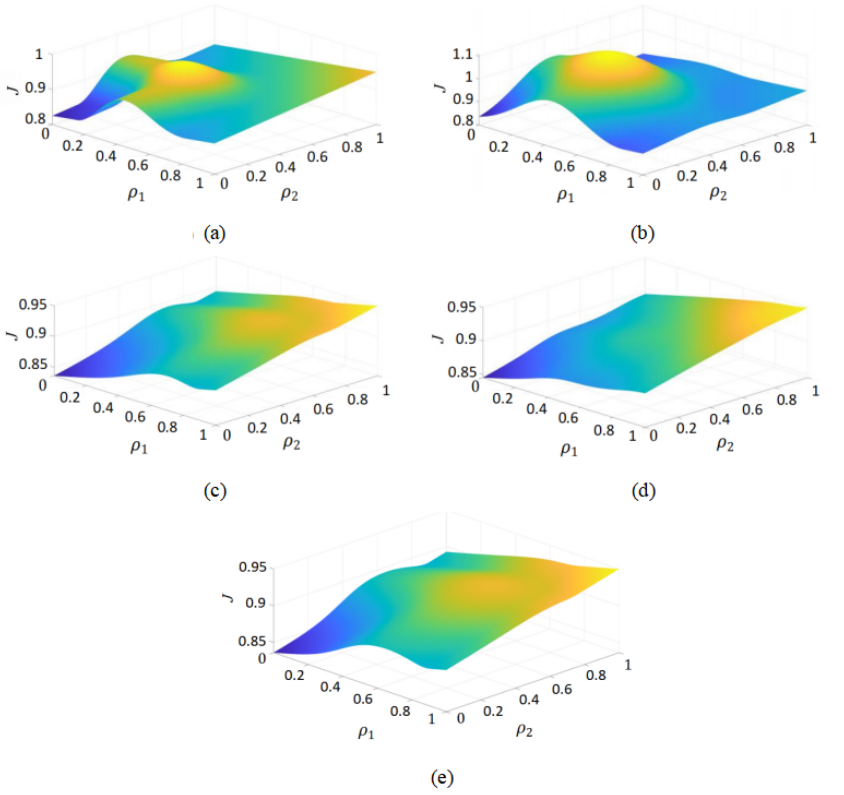

Fig. 7 Objective function of the augmented Lagrangian method under different constraint relaxations

and the polynomial vanishing constraint are expected to impose harsher punishment on the regions that violate the constraints, as shown in Fig. 7(d) and Fig. 7(e).

Fig. 8 shows the optimization iterations of the simple example using qp-relaxation ($q - p = 0.5$), SIMP-type cubic constraints and polynomial vanishing constraints starting from two different initial points $\boldsymbol{\rho} = [0.5\,;\ 0.6]$ and $\boldsymbol{\rho} = [0.6\,;\ 0.5]$. It can be found that except for the second constraint form the other two methods can converge to the global optimum. However, the qp - approach changes the value of the global optimum from 0.8236 to 0.7514. It is worth pointing out that the qp - approach or ϵ-relaxation enables the optimizer, such as MMA, to reach the global optimum by opening the feasible domain when facing the singular optimum problems. While when the polynomial vanishing constraints are applied in the AL method, they not only retains the characteristics of the original constraint, but also makes the result converge to the global optimum.

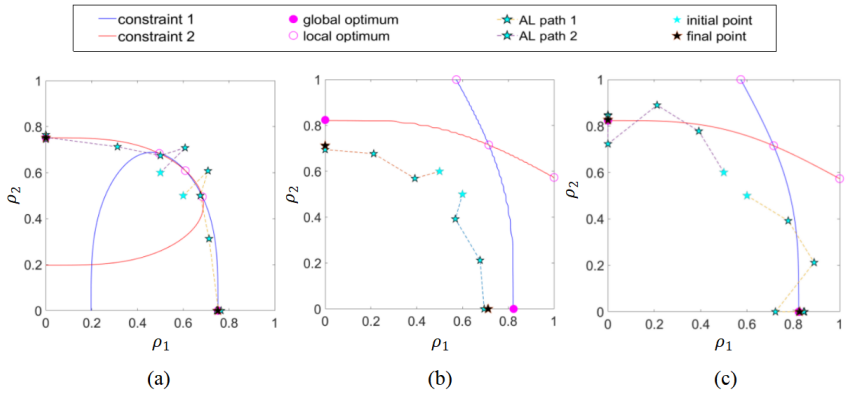

Fig. 8 Optimization iterative process under (a) qp - relaxation, (b) SIMP-type cubic constraint and (c) polynomial vanishing constraint

5 Numerical results

Several numerical results obtained through MATLAB are given in this section to demonstrate the characteristics of the proposed method. In particular, its performance is compared to the *PolyStress* (Giraldo-Londoño and Paulino [39]) in terms of discretization, mesh sensitivity and computational efficiency when the von Mises stress constraints are applied. Table 1 shows the parameters used in this study and they apply to all examples if not specifically stated.

Table 1 Input parameters used in this study

Parameter	Description	Value
$\boldsymbol{\rho}^{(0)}$	Initial density vector	$\mathbf{0.5}$
β	Initial Heaviside projection penalization factor	1
$\beta_{\max}$	Maximum Heaviside projection penalty factor	10
η	Heaviside projection threshold	0.5
$\boldsymbol{\lambda}^{(0)}$	Initial Lagrange multiplier vector	$\mathbf{0}$
$\mu^{(0)}$	Initial penalty coefficient	10
α	Penalty factor updating parameter	1.05
q	Nonlinear filter index	3.5
δ	Convergence tolerance of design variables for AL	0.005
δ_s	Convergence tolerance of stress constraints for AL	0.005
$MaxIter$	Maximum number of external loops	150
$MaxInAL$	Maximum number of internal loops per AL step	5

5.1 2D L-bracket

The L-bracket topology optimization problem is one of the most extensively studied problems in the literature. The design domain and boundary conditions

are shown in Fig. 9. The model is fully constrained at the top left edge, and the distributed load $\boldsymbol{f}$ is applied at the top right free end along a distance d. The material characteristics, geometric shapes and loading conditions used in this example and shown in Table 2 are consistent with the reference [39].

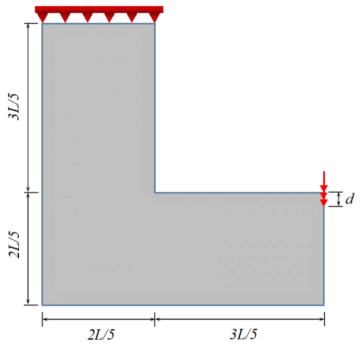

Fig. 9 Design domain and boundary conditions of 2D L-bracket problem

Table 2 Parameters for the 2D L-bracket problem

Parameter	Description	Value
E_0	Young's modulus	70 GPa
μ	Poisson's ratio	0.25
$\bar{\sigma}$	Yield stress	100 MPa
L	Length	100 mm
t	Thickness	1 mm
f	Applied load	200 N
d	Load distribution distance	6 mm
R	Density filter radius	5 mm

To test the mesh sensitivity, two clouds of regularly spaced nodes, 10251 and 40501, are generated. In Fig. 10, the topology optimization results are compared with the same problem, which is solved by *PolyStress* with the same node distribution. The results obtained by both codes are well consistent.

Table 3 Comparison between *PolyStress* and CNEM

	PolyStress		CNEM	
Nodal size	Main loop time	Objective function	Main loop time	Objective function
10251	23 seconds	31.6%	72 seconds	33.2%
40501	132 seconds	33.2%	342 seconds	32.8%

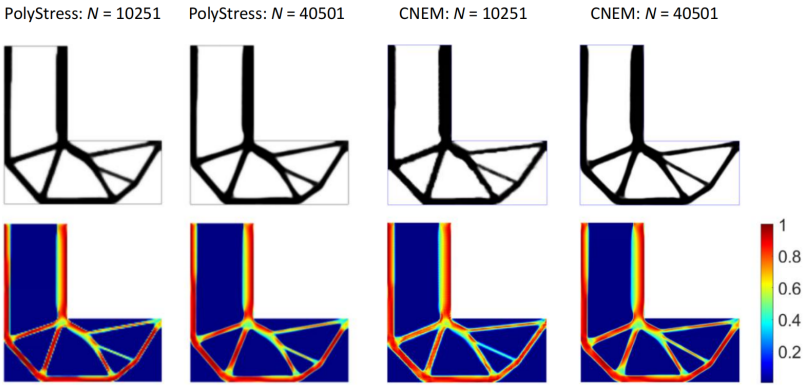

Fig. 10 L-shaped topologies and normalized von Mises stress maps under different levels of mesh refinement for *PolyStress* and CNEM

The optimization iterations are run by MATLAB R2021a on a computer with a 2.60 GHz processor. The computation times shown in Table 3 include only the time consumed by the main loop, excluding the pre-processing time. The CNEM requires more time to achieve convergence than *PolyStress*. This is due to the fact that each node in CNEM has more neighbor nodes to construct the interpolation functions, resulting in larger strain-displacement matrix and a wider bandwidth for the stiffness matrix, which consumes more time in equilibrium equation solving and sensitivity analysis.

Although not as economical as *PolyStress* in terms of computation time, CNEM is able to produce smoother stress maps compared to the jagged stresses at the structure boundaries in *PolyStress*, as shown in Fig. 11. More importantly, CNEM is largely unaffected by discretization and is able to produce similar results even in irregular Voronoi cells.

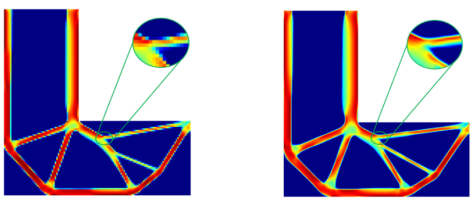

Fig. 11 Details of von Mises stress maps for PolyStress (left) and CNEM (right)

In Fig. 12, the results obtained using density-based filters and neighbor-based filters are compared in highly irregular discretization case. It can be observed that small branches appear for the density filter when the radius is smaller while the neighbor-based filters provide the same output for different number of layers considered.

Typically, designs generated by topology optimization often include free-form and complex shapes that are complicated or cannot be manufactured

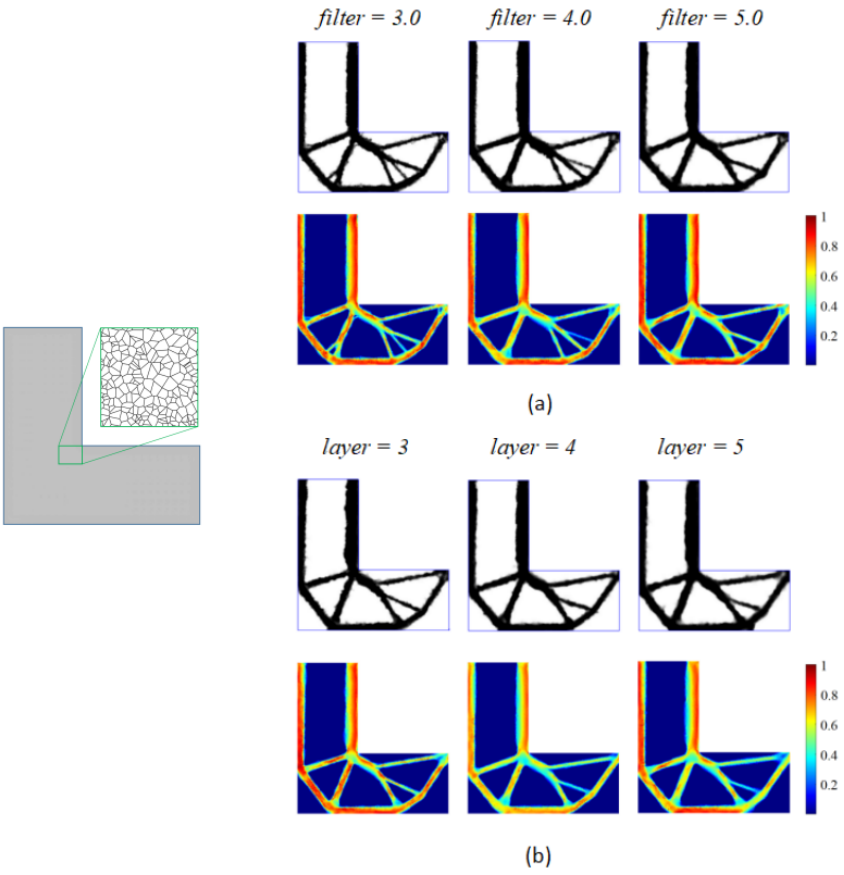

Fig. 12 L-bracket topologies and normalized von Mises stress maps under irregular discretization (left) obtained by (a) density filter and (b) neighbor-based filter

using traditional manufacturing methods. However, topology optimization designs are well suited for additive manufacturing processes that have more relaxed design rules and can easily replicate complex shapes without additional cost. Therefore, for the subsequent topology optimization analysis in this paper, the parameters of the additive manufactured Ti-6Al-4V alloy structure are considered. Their mechanical and fatigue parameters come from the references (Mower and Long [61]; Fatemi et al. [62]) and are listed in Table 4.

Fig. 13 shows the results of topology optimization subjected to Crossland fatigue constraints under a sinusoidal distributed load with an amplitude of 850 N and a mean value of 0. It can be seen that the fatigue constraint is satisfied everywhere and the maximum von Mises stress is much lower than the yield stress. As mentioned before, the von Mises stress constraint is a simplified case of the Crossland fatigue constraint, therefore a closer topology is obtained when the same optimizer and parameters are used.

Table 4 Mechanical and fatigue parameters for Ti-6Al-4V alloy

Parameter	Description	Value
E_0	Young's modulus	100 GPa
μ	Poisson's ratio	0.25
$\bar{\sigma}$	Yield stress	1000 MPa
f_{-1}	fully reversed bending fatigue limit	454 MPa
t_{-1}	fully reversed torsional fatigue limit	300 MPa

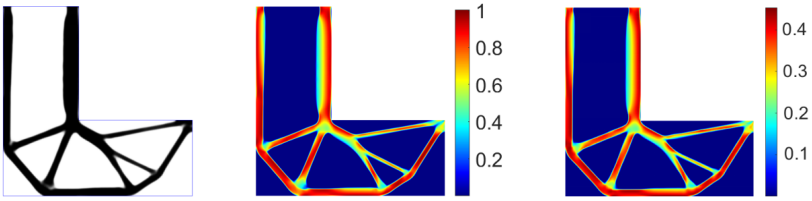

Fig. 13 L-bracket topology (left), normalized Crossland fatigue constriant (middle) and normalized von Mises stress (right) maps

5.2 2D portal frame

The second optimization problem is a portal frame with the geometry and boundary conditions shown in Fig. 14. The parameters applied for this benchmark are listed in Table 5. The domain is discretized using three different numbers of elements, which are respectively composed of polygonal finite elements generated by *PolyStress* and Voronoi cells generated by CNEM. The topologies and stress maps shown in Fig. 15 are obtained by using a filter radius $R = 6mm$ by CNEM. In order to obtain symmetric solutions, the design variables on the left and right sides of the two programs are symmetrized during the optimization.

Table 5 Parameters for the 2D portal frame problem

Parameter	Description	Value
L	Length	120 mm
H	Height	60 mm
h	Concave height	35 mm
b	Bearing length	5.5 mm
t	Thickness	1 mm
f	Applied load	3000 N
d	Load distribution distance	10 mm
R	Density filter radius	6 mm

Within *PolyStress*, the complexity of this design domain requires a series of iterations in pre-processing to generate high quality polygonal finite elements. The results shown in Fig. 16 correspond to different number of elements generated by 10, 50 and 100 iterations, respectively.

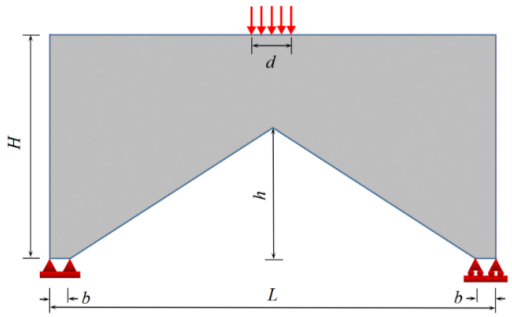

Fig. 14 Design domain and boundary conditions of 2D portal frame problem

It is evident from the results that the stress constraints are always locally satisfied for both programs within the framework of the AL-based approach. The topologies obtained by CNEM are very similar across all levels of mesh refinement and degree of regularity of the mesh. However, in *PolyStress*, the optimized results are affected not only by the mesh refinement but also by the mesh quality. These differences are mainly reflected in the bottom of the support bars and the way of the bar connections in the truss structure above. When using the discrete scheme $N = 92809$, the results obtained are closer to those of CNEM, but this does not mean that the results will be further improved with the refinement of the mesh. In addition, excessive iteration is not necessarily better. For example, a solution with 50 iterations may give better results than 100 iterations when $N = 133484$.

Finally, the topology optimization of the Ti-6Al-4V alloy portal frame subjected to the Crossland fatigue criterion is plotted in Fig. 17, where the amplitude and mean value of the sinusoidal cyclic loading are 1400N and 0N, respectively. Similarly, the maximum von Mises stress of the optimized structure is less than the yield stress. More interestingly, when incorporating both the von Mises stress constraint and the Crossland fatigue constraint into the topology optimization, the final result is consistent with the optimization subject to the fatigue constraint only.

5.3 2D eyebar

The Crossland fatigue criterion constrained topology optimization designs in the above two cases are very similar to the stress-constrained designs under single loading conditions. In order to introduce small visible difference due to the hydrostatic stress, a problem commonly referred to as a eyebar is solved here. The problems similar to this benchmark can also be found in the references [39, 63]. The geometry and boundary conditions of the eyebar problem are plotted in Fig. 18. The left side of the hole is subjected to a horizontal load $\boldsymbol{f}$, which is distributed according to the function as follows:

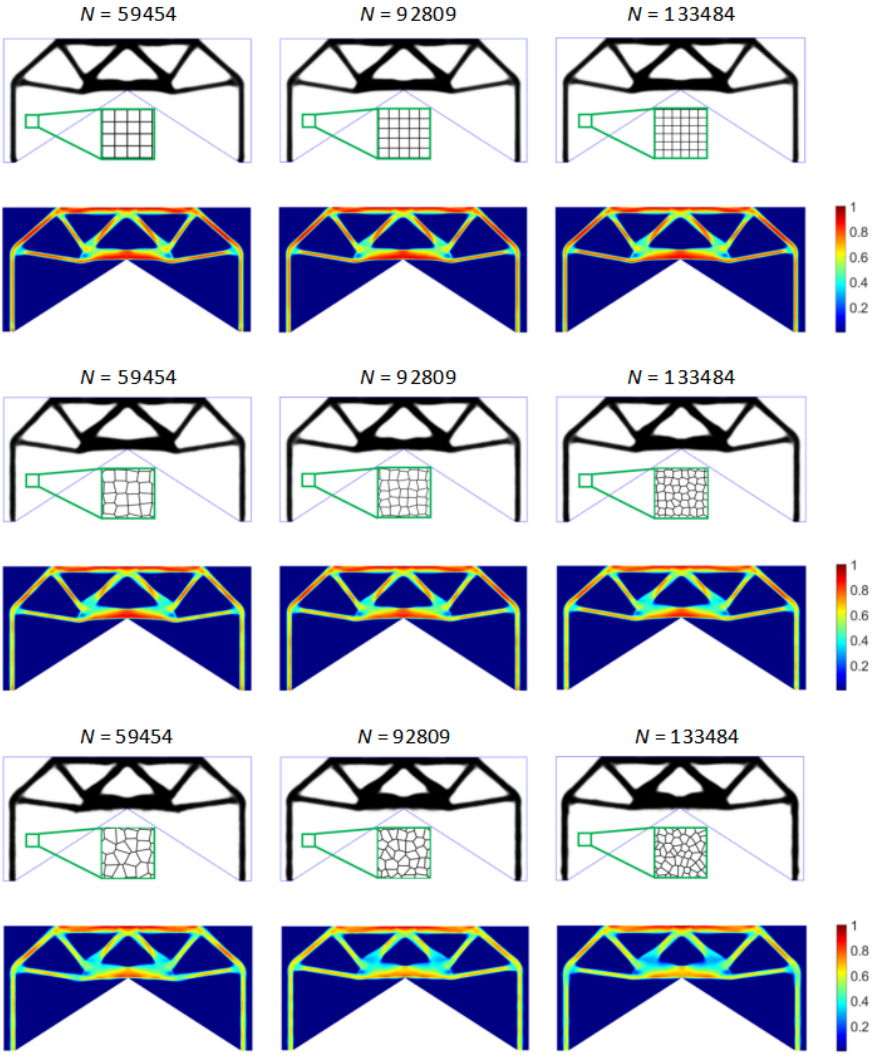

Fig. 15 Topologies and normalized von Mises stress maps for several discretization schemes by CNEM

$$f = w\left(r^2 - y^2\right) \tag{24}$$

where w is a factor that adjusts the load amplitude according to the hole radius r and the vertical coordinate y. In this case, w equals to 1.6 and 0.8 in the stress-constrained and fatigue-constrained problems, respectively. The vertical coordinate of the hole center in this problem is 0, thus the distributed load decreases towards the top and bottom sides.

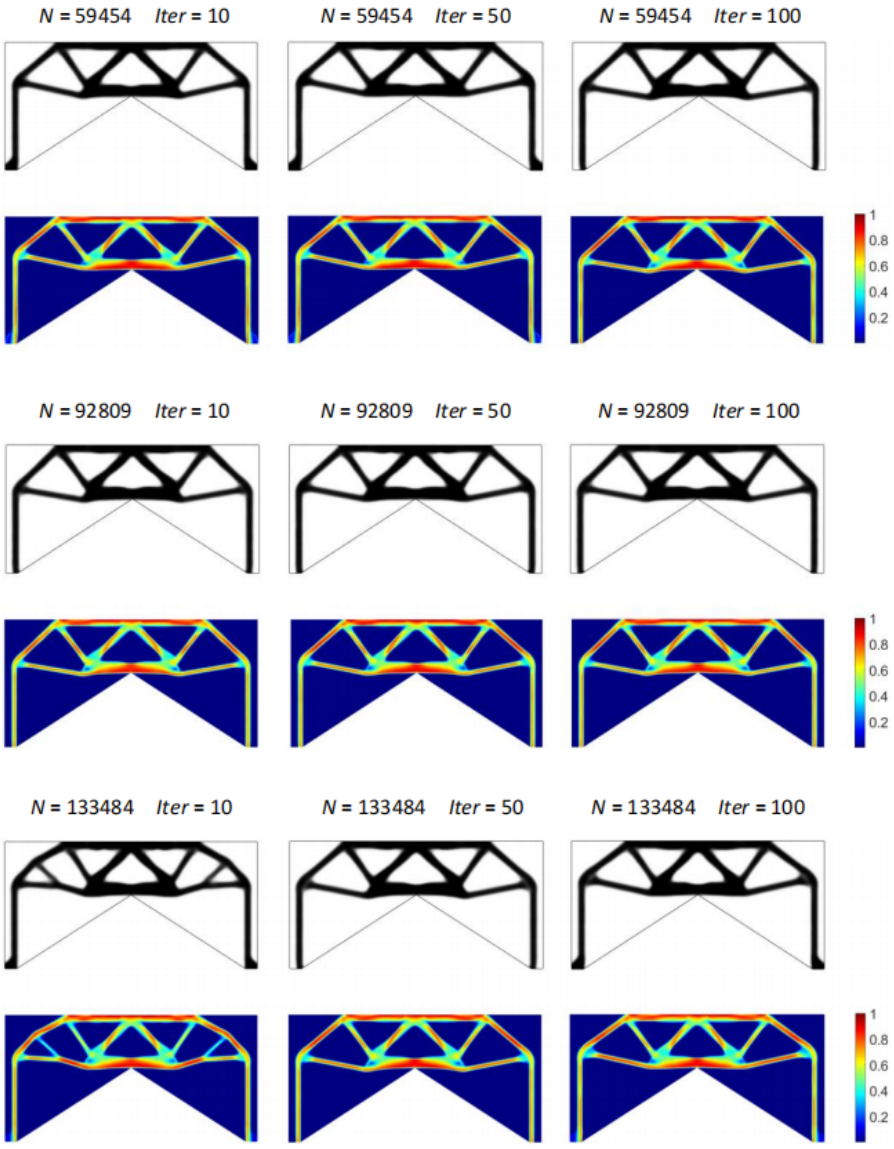

Fig. 16 Topologies and normalized von Mises stress maps of several discretization schemes with different iterations in by PolyStress

For this problem, the parameters used are shown in Table 6 and the material parameters considered is additive manufactured Ti-6Al-4V alloy. The entire design domain is discretized using $N = 49056$ Voronoi cells and the topology optimization results based on von Mises stress and Crossland fatigue criterion constraints are shown in Fig. 19. It can be noticed that the two optimized results present approximately the same contour and two small holes

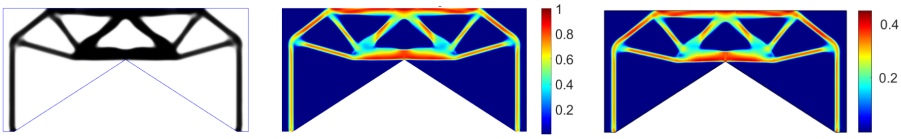

Fig. 17 Portal frame topology (left), normalized Crossland fatigue constriant (middle) and normalized von Mises stress (right) maps

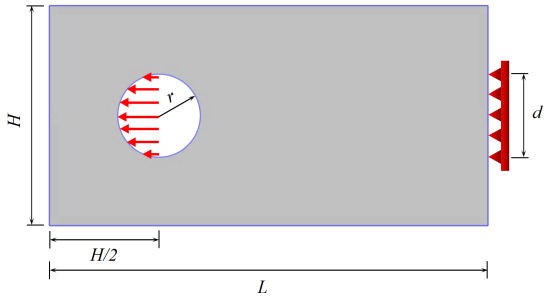

Fig. 18 Design domain and boundary conditions of 2D eyebar problem

Table 6 Parameters for the 2D eyebar problem

Parameter	Description	Value
L	Length	160 mm
H	Height	80 mm
r	Hole radius	15 mm
t	Thickness	1 mm
d	Constraint distance	30 mm
R	Density filter radius	4 mm

appear on the left position of the loaded part of the boundary domain. However, different connecting rods are used on the right side of the hole, i.e., one vertical rod in the stress-constrained problem and two curved rods connected to each other with fatigue constraints.

6 Conclusion

In this paper, a framework for topology optimization considering stress and fatigue constraints is proposed. It combines the CNEM to solve the equilibrium equations and the AL to solve the local minimum problem. Due to the characteristics of CNEM, rapid discretization of any design domain has become realistic, which provides a lot of convenience for the pre-processing part of the program. Before the main optimization loop, it is only necessary to lay out the node distribution and generate the unique corresponding constrained Voronoi diagram. This process does not need any iteration nor consider the quality of

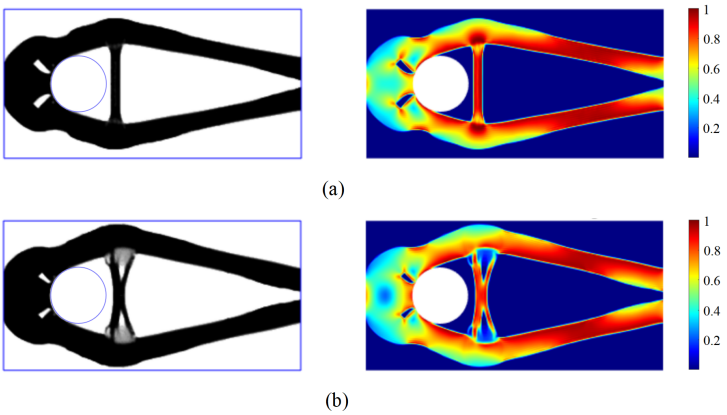

Fig. 19 Eyebar topologies and normalized constraint maps under (a) von Mises stress constraints and (b) Crossland criterion constraints

the Voronoi cell. Moreover, the construction of the neighbor-based interpolation function is purely geometric and does not involve any artificially defined parameters.

Like many meshless methods, the stiffness matrix in CNEM has a wider bandwidth, which makes the sensitivity analysis of the program become expensive, but importantly, it can achieve robust topology output under various discretization conditions, including regular and irregular ones. In particular, the proposed method is expected to achieve greater potential in topology optimization problems for complex design domains. For the FEM, it has great advantageous to perform topology optimization in regular design domains, but in non-regular geometries, a series of iterations are required to generate a high-quality mesh, and the relationship between the number of iterations and the optimization results is not clear yet.

Generally speaking, topology optimization with stress or fatigue constraints is still an open problem, lacking an effective and robust methodology to solve large-scale problems with local constraints. It is also necessary to point out that the present method does not guarantee to find a global optimal solution. This is actually determined not only by the optimization algorithm, but also by the formulation of the design problem. Therefore, the future expansion of the current work includes the implementation of other advanced optimizers, such as machine learning and deep learning to speed up the design process. In addition, the fatigue criteria based on stress invariants cannot specify the direction of potential fatigue cracks and their applicability is limited to the case where the main axis of the alternating stress is fixed to the object. The next step of this study also includes the implementation of fatigue criteria based on critical plane theory into topology optimization.

7 Conflict of interest statement

On behalf of all authors, the corresponding author states that there is no conflict of interest.

8 Replication of results

To reproduce the optimized results described above, the equilibrium equation can be solved by CNEM in Section 2. The local minimum problem can be solved using the modified AL formula [39]. The sensitivities are derived in Appendices A and B and the relevant parameters are given in Table 1.

9 Acknowledgments

The authors acknowledge the financial support from "China Scholarship Council (CSC)" under the project titled "Topology optimization of additive manufactured parts including fatigue behavior".

Appendix A Sensitivity analysis of stress-constrained topology optimization

The sensitivity of the AL function in Eq. 19 at k-th iteration can be obtained as:

$$\frac{\partial J}{\partial \rho_i} = \sum_{j=1}^{N} \left(\frac{\partial f}{\partial \tilde{\rho}_j} \frac{d\tilde{\rho}_j}{d\rho_i} + \frac{1}{N} \frac{\partial P}{\partial \tilde{\rho}_j} \frac{d\tilde{\rho}_j}{d\rho_i} \right) \tag{A1}$$

where

$$P^{(k)}(\overline{\boldsymbol{\rho}}, \boldsymbol{u}) = \sum_{j=1}^{N} \left[\lambda_j^{(k)} h_j(\overline{\boldsymbol{\rho}}, \boldsymbol{u}) + \frac{\mu^{(k)}}{2} h_j(\overline{\boldsymbol{\rho}}, \boldsymbol{u})^2 \right] \tag{A2}$$

is the penalization term.

For the first item on the right side of Eq. A1, $d\tilde{\rho}_j/d\rho_i = \mathcal{F}_{ji}$ is obtained from the filter relation in Eq. 10 and the term $df/d\tilde{\rho}_j$ is given by:

$$\frac{\partial f}{\partial \tilde{\rho}_j} = \frac{\partial}{\partial \tilde{\rho}_j} \frac{\sum_{i=1}^{N} \bar{\rho}_i V_i}{|\Omega|} = \frac{V_j}{|\Omega|} \frac{d\bar{\rho}_j}{d\tilde{\rho}_j} = \frac{V_j}{|\Omega|} \frac{\beta \left[1 - \tanh\left(\beta\left(\tilde{\rho}_j - \eta\right)\right)\right]^2}{\tanh(\beta\eta) + \tanh[\beta(1-\eta)]} \tag{A3}$$

The calculation of the second term $\partial P/\partial \tilde{\rho}_i$ in Eq. A1 is expressed as follows:

$$\frac{\partial P^{(k)}}{\partial \tilde{\rho}_j} = \sum_{i=1}^{N} \left[\lambda_i^{(k)} + \mu^{(k)} h_i\right] \frac{\partial h_i}{\partial \tilde{\rho}_j} \tag{A4}$$

Based on Eq. 20 and Eq. 23e, the non zero part of Eq. A4 is determined as:

$$\begin{aligned} \frac{\partial h_i}{\partial \tilde{\rho}_j} &= p(1-\epsilon)\bar{\rho}_i^{p-1}\delta_{ij} g_i \left(g_i^2 + 1\right) \frac{d\bar{\rho}_i}{d\tilde{\rho}_i} \\ &+ \frac{\epsilon + (1-\epsilon)\bar{\rho}_i^p}{\sigma_{lim}} \left(3{g_i}^2 + 1\right) \left(\frac{\partial \sigma_{vm}^i}{\partial \boldsymbol{u}}\right)^T \frac{\partial \boldsymbol{u}}{\partial \tilde{\rho}_j} \end{aligned} \tag{A5}$$

when $\widetilde{g}_i(\overline{\boldsymbol{\rho}}) \geq -\lambda_i^{(k)}/\mu^{(k)}$, otherwise $\partial h_i/\partial \tilde{\rho}_j = 0$.

The adjoint method is used here to reduce the cost of sensitivity evaluation, then $\partial P^{(k)}/\partial \tilde{\rho}_j$ is calculated as:

$$\frac{\partial P^{(k)}}{\partial \tilde{\rho}_j} = \left[\lambda_j^{(k)} + \mu^{(k)} h_j\right] p(1-\epsilon)\bar{\rho}_j^{p-1} g_j \left(g_j^2 + 1\right) \frac{d\bar{\rho}_j}{d\tilde{\rho}_j} + \boldsymbol{\eta}^T \frac{\partial \boldsymbol{K}}{\partial \tilde{\rho}_j} \boldsymbol{u} \tag{A6}$$

with the adjoint problem:

$$\boldsymbol{\eta}^T \boldsymbol{K} = -\sum_{i=1}^{N} \left[\lambda_i^{(k)} + \mu^{(k)} h_i\right] \frac{\epsilon + (1-\epsilon)\bar{\rho}_i^p}{\sigma_{lim}} \left(3{g_i}^2 + 1\right) \left(\frac{\partial g_i}{\partial \boldsymbol{u}}\right) \tag{A7}$$

Since the stiffness matrix is constructed through Eq. 13, the second part on the right of Eq. A6 can be calculated as:

$$\boldsymbol{\eta}^T \frac{\partial K}{\partial \tilde{\rho}_j} \boldsymbol{u} = \boldsymbol{\eta}_j^T \frac{\partial \boldsymbol{K}_j}{\partial \tilde{\rho}_j} \boldsymbol{u}_j = p(1-\epsilon)\bar{\rho}_j^{p-1} \boldsymbol{\eta}_j^T \boldsymbol{K}_{j0} \boldsymbol{u}_j \frac{d\bar{\rho}_j}{d\tilde{\rho}_j} \tag{A8}$$

The sensitivity of von Mises stress to the Cauchy stress vector is equal to:

$$\frac{\partial \sigma_{vm}^j}{\partial \boldsymbol{\sigma}} = \frac{\boldsymbol{M}\boldsymbol{\sigma}}{\sigma_{vm}^j} \tag{A9}$$

The term $\partial \boldsymbol{\sigma}/\partial \boldsymbol{u}$ can be deduced through Eq. 6:

$$\frac{\partial \boldsymbol{\sigma}}{\partial \boldsymbol{u}} = \boldsymbol{C}\boldsymbol{B} \tag{A10}$$

Finally, we obtain the following:

$$\frac{\partial J}{\partial \rho_i} = \left(\boldsymbol{\mathcal{F}}^T\right)_i \left\{ \frac{V_i}{|\Omega|} + \frac{1}{N} \left[\left(\lambda_i^{(k)} + \mu^{(k)} h_i \right) p(1-\epsilon) \bar{\rho}_i^{p-1} g_i \left(g_i^2 + 1 \right) \right. \right. \\ \left. \left. + \; p(1-\epsilon) \bar{\rho}_i^{p-1} \boldsymbol{\eta}_i^T \boldsymbol{K}_{i0} \boldsymbol{u}_i \right] \right\} \frac{\beta \left[1 - \tanh\left(\beta\left(\tilde{\rho}_j - \eta\right)\right)\right]^2}{\tanh(\beta\eta) + \tanh[\beta(1-\eta)]} \tag{A11}$$

where $\boldsymbol{\mathcal{F}}_i$ is the i-th row of the filter matrix.

Appendix B Sensitivity analysis of fatigue constrained topology optimization

The AL-based method for topology optimization with fatigue constraints is similar to that with stress constraints, the main difference being that the load is cyclic in this case. Since the solid mechanics problem is linear elastic in this study, the relationships between the displacements and stresses obtained at each moment are also linear. Therefore, the equilibrium equation at any time point multiplied by an arbitrary adjoint vector $\boldsymbol{\eta}$ is added to the penalization term when the adjoint method is used for sensitivity analysis:

$$\frac{\partial P^{(k)}}{\partial \tilde{\rho}_j} = \left[\lambda_j^{(k)} + \mu^{(k)} h_j \right] p(1-\epsilon) \bar{\rho}_j^{p-1} g_j \left(g_j^2 + 1 \right) \frac{d\bar{\rho}_j}{d\tilde{\rho}_j} + \boldsymbol{\eta}^T \frac{\partial \boldsymbol{K}}{\partial \tilde{\rho}_j} \boldsymbol{u}_{ref} \tag{B12}$$

where $\boldsymbol{u}_{ref}$ represents the reference displacement vector at any predetermined loading moment. The adjoint problem then becomes:

$$\boldsymbol{\eta}^T \boldsymbol{K} = -\sum_{i=1}^{N} \left[\lambda_i^{(k)} + \mu^{(k)} h_i \right] \left(\frac{\partial h_i}{\partial \boldsymbol{u}_{ref}} \right) \tag{B13}$$

when $\widetilde{g}_i(\overline{\boldsymbol{\rho}}) \geq -\lambda_i^{(k)}/\mu^{(k)}$, $\partial h_i / \partial \boldsymbol{u}_{ref}$ is expressed as follows:

$$\frac{\partial h_j}{\partial \boldsymbol{u}_{ref}} = \frac{\partial \widetilde{g}_i}{\partial \sqrt{J_{2,a}^j}} \frac{\partial \sqrt{J_{2,a}^j}}{\partial \boldsymbol{\sigma}_a} \frac{\partial \boldsymbol{\sigma}_a}{\partial \boldsymbol{u}_{ref}} + \frac{\partial \widetilde{g}_i}{\partial \sigma_{H,\,\max}^j} \frac{\partial \sigma_{H,\,\max}^j}{\partial \sigma_{H,ref}^j} \frac{\partial \sigma_{H,ref}^j}{\partial \boldsymbol{\sigma}_{ref}} \frac{\partial \boldsymbol{\sigma}_{ref}}{\partial \boldsymbol{u}_{ref}} \tag{B14}$$

where $\boldsymbol{\sigma}_{H,ref}$ and $\boldsymbol{\sigma}_{ref}$ respectively represent the reference hydrostatic stress vector and the reference stress vector at any given reference time. Based on Eq. 14 and Eq. 23e, the sensitivity of the constraint $\boldsymbol{g}$ to the $\sqrt{J_{2,a}^j}$ and the $\boldsymbol{\sigma}_{H,max}$ of Voronoi cell j are:

$$\begin{cases} \dfrac{\partial \widetilde{g}_i}{\partial \sqrt{J^j_{2,a}}} = \dfrac{p(1-\epsilon)\bar{\rho}_j^{p-1}\left(3g_j^2+1\right)}{\beta_c} \\ \dfrac{\partial \widetilde{g}_i}{\partial \sigma^j_{H,\max}} = \dfrac{\alpha_c p(1-\epsilon)\bar{\rho}_j^{p-1}\left(3g_j^2+1\right)}{\beta_c} \end{cases} \tag{B15}$$

The term $\partial\sqrt{J^j_{2,a}}/\partial\boldsymbol{\sigma}_a$ in Eq. B15 is similar with Eq. A9, where $\partial\sqrt{J^j_{2,a}}/\partial\boldsymbol{\sigma}_a = \boldsymbol{M}_c\boldsymbol{\sigma}_a/\sqrt{J^j_{2,a}}$.

The sensitivity of the stress amplitude to the reference displacement can be expressed as:

$$\begin{aligned} \frac{\partial \boldsymbol{\sigma}_a}{\partial \boldsymbol{u}_{ref}} &= \frac{1}{2}\left(\frac{\partial \boldsymbol{\sigma}_{max}}{\partial \boldsymbol{u}_{ref}} - \frac{\partial \boldsymbol{\sigma}_{min}}{\partial \boldsymbol{u}_{ref}}\right) = \frac{1}{2}\left(\frac{\partial \boldsymbol{\gamma}_1\boldsymbol{\sigma}_{ref}}{\partial \boldsymbol{u}_{ref}} - \frac{\partial \boldsymbol{\gamma}_2\boldsymbol{\sigma}_{ref}}{\partial \boldsymbol{u}_{ref}}\right) \\ &= \frac{1}{2}\left(\boldsymbol{\gamma_1} - \boldsymbol{\gamma_2}\right)\boldsymbol{CB} \end{aligned} \tag{B16}$$

where $\boldsymbol{\gamma}_1 = \boldsymbol{\sigma}_{max}/\boldsymbol{\sigma}_{ref}$ and $\boldsymbol{\gamma}_2 = \boldsymbol{\sigma}_{min}/\boldsymbol{\sigma}_{ref}$ are coefficient vectors.

For 2D plane stress state, $\partial\boldsymbol{\sigma}^j_{H,ref}/\partial\boldsymbol{\sigma}^j_{ref} = \left[\,1/3\ \ 1/3\ \ 0\,\right]^T$.

References

[1] Michell, A.G.M.: The limits of economy of material in frame-structures. The London, Edinburgh, and Dublin Philosophical Magazine and Journal of Science **8**(47), 589–597 (1904). https://doi.org/10.1080/14786440409463229

[2] Prager, W., Rozvany, G.I.N.: Optimization of structural geometry. In: Bednarek, A.R., Cesari, L. (eds.) Dynamical Systems, pp. 265–293. Academic Press, Florida (1977). https://doi.org/10.1016/B978-0-12-083750-2.50023-0

[3] Rozvany, G.I.N.: Optimal layout theory: Analytical solutions for elastic structures with several deflection constraints and load conditions. Structural optimization **4**(3), 247–249 (1992). https://doi.org/10.1007/BF01742753

[4] Bendsøe, M.P., Kikuchi, N.: Generating optimal topologies in structural design using a homogenization method. Computer Methods in Applied Mechanics and Engineering **71**(2), 197–224 (1988). https://doi.org/10.1016/0045-7825(88)90086-2

[5] Ferrari, F., Sigmund, O.: A new generation 99 line Matlab code for compliance topology optimization and its extension to 3D. Structural and

Multidisciplinary Optimization **62**(4), 2211–2228 (2020). https://doi.org/10.1007/s00158-020-02629-w

[6] Xia, L., Xia, Q., Huang, X., Xie, Y.M.: Bi-directional Evolutionary Structural Optimization on Advanced Structures and Materials: A Comprehensive Review. Archives of Computational Methods in Engineering **25**(2), 437–478 (2018). https://doi.org/10.1007/s11831-016-9203-2

[7] Wallin, M., Ristinmaa, M.: Boundary effects in a phase-field approach to topology optimization. Computer Methods in Applied Mechanics and Engineering **278**, 145–159 (2014). https://doi.org/10.1016/j.cma.2014.05.012

[8] Sigmund, O., Maute, K.: Topology optimization approaches. Structural and Multidisciplinary Optimization **48**(6), 1031–1055 (2013). https://doi.org/10.1007/s00158-013-0978-6

[9] Díaz, A., Sigmund, O.: Checkerboard patterns in layout optimization. Structural optimization **10**(1), 40–45 (1995). https://doi.org/10.1007/BF01743693

[10] Jang, G.-W., Jeong, J.H., Kim, Y.Y., Sheen, D., Park, C., Kim, M.-N.: Checkerboard-free topology optimization using non-conforming finite elements. International Journal for Numerical Methods in Engineering **57**(12), 1717–1735 (2003). https://doi.org/10.1002/nme.738

[11] Matsui, K., Terada, K.: Continuous approximation of material distribution for topology optimization. International Journal for Numerical Methods in Engineering **59**(14), 1925–1944 (2004). https://doi.org/10.1002/nme.945

[12] Paulino, G.H., Le, C.H.: A modified Q4/Q4 element for topology optimization. Structural and Multidisciplinary Optimization **37**(3), 255–264 (2009). https://doi.org/10.1007/s00158-008-0228-5

[13] Talischi, C., Paulino, G.H., Le, C.H.: Honeycomb wachspress finite elements for structural topology optimization. Structural and Multidisciplinary Optimization **37**(6), 569–583 (2009). https://doi.org/10.1007/s00158-008-0261-4

[14] Talischi, C., Paulino, G.H., Pereira, A., Menezes, I.F.M.: Polygonal finite elements for topology optimization: A unifying paradigm. International Journal for Numerical Methods in Engineering **82**(6), 671–698 (2010). https://doi.org/10.1002/nme.2763

[15] Talischi, C., Paulino, G.H., Pereira, A., Menezes, I.F.M.: Polytop: a matlab implementation of a general topology optimization framework using

unstructured polygonal finite element meshes. Structural and Multidisciplinary Optimization **45**(3), 329–357 (2012). https://doi.org/10.1007/s00158-011-0696-x

[16] Ullah, B., Trevelyan, J.: A boundary element and level set based topology optimisation using sensitivity analysis. Engineering Analysis with Boundary Elements **70**, 80–98 (2016). https://doi.org/10.1016/j.enganabound.2016.06.001

[17] Oliveira, H.L., Leonel, E.D.: Boundary element method applied to topology optimization using the level set method and an alternative velocity regularization. Meccanica **54**(3), 549–563 (2019). https://doi.org/10.1007/s11012-019-00954-z

[18] Simonetti, H.L., Almeida, V.S., de Assis das Neves, F., Greco, M.: Multiobjective topology optimization using the Boundary Element Method. Structures **19**, 84–95 (2019). https://doi.org/10.1016/j.istruc.2018.12.002

[19] Cho, S., Kwak, J.: Topology design optimization of geometrically nonlinear structures using meshfree method. Computer Methods in Applied Mechanics and Engineering **195**(44), 5909–5925 (2006). https://doi.org/10.1016/j.cma.2005.08.015

[20] Zhou, J.X., Zou, W.: Meshless approximation combined with implicit topology description for optimization of continua. Structural and Multidisciplinary Optimization **36**(4), 347–353 (2008). https://doi.org/10.1007/s00158-007-0168-5

[21] Wang, Y., Luo, Z., Wu, J., Zhang, N.: Topology optimization of compliant mechanisms using element-free Galerkin method. Advances in Engineering Software **85**, 61–72 (2015). https://doi.org/10.1016/j.advengsoft.2015.03.001

[22] Li, S., Atluri, S.: Topology-optimization of Structures Based on the MLPG Mixed Collocation Method. Computer Modeling in Engineering & Sciences **26**(1), 61–74 (1970). https://doi.org/10.3970/cmes.2008.026.061

[23] Shobeiri, V.: Topology optimization using bi-directional evolutionary structural optimization based on the element-free Galerkin method. Engineering Optimization **48**(3), 380–396 (2016). https://doi.org/10.1080/0305215X.2015.1012076

[24] Luo, Z., Zhang, N., Gao, W., Ma, H.: Structural shape and topology optimization using a meshless Galerkin level set method. International Journal for Numerical Methods in Engineering **90**(3), 369–389 (2012). https://doi.org/10.1002/nme.3325

[25] Neofytou, A., Picelli, R., Huang, T.-H., Chen, J.-S., Kim, H.A.: Level set topology optimization for design-dependent pressure loads using the reproducing kernel particle method. Structural and Multidisciplinary Optimization **61**(5), 1805–1820 (2020). https://doi.org/10.1007/s00158-020-02549-9

[26] Rozvany, G.I.N.: Difficulties in truss topology optimization with stress, local buckling and system stability constraints. Structural optimization **11**(3), 213–217 (1996). https://doi.org/10.1007/BF01197036

[27] Duysinx, P., Bendsøe, M.P.: Topology optimization of continuum structures with local stress constraints. International Journal for Numerical Methods in Engineering **43**(8), 1453–1478 (1998). https://doi.org/10.1002/(SICI)1097-0207(19981230)43:8⟨1453::AID-NME480⟩3.0.CO;2-2

[28] Cheng, G.D., Guo, X.: ε-relaxed approach in structural topology optimization. Structural optimization **13**(4), 258–266 (1997). https://doi.org/10.1007/BF01197454

[29] París, J., Navarrina, F., Colominas, I., Casteleiro, M.: Topology optimization of continuum structures with local and global stress constraints. Structural and Multidisciplinary Optimization **39**(4), 419–437 (2009). https://doi.org/10.1007/s00158-008-0336-2

[30] Bruggi, M.: On an alternative approach to stress constraints relaxation in topology optimization. Structural and Multidisciplinary Optimization **36**(2), 125–141 (2008). https://doi.org/10.1007/s00158-007-0203-6

[31] Kreisselmeier, G., Steinhauser, R.: Systematic control design by optimizing a vector performance index. IFAC Proceedings Volumes **12**(7), 113–117 (1979). https://doi.org/10.1016/S1474-6670(17)65584-8

[32] Le, C., Norato, J., Bruns, T., Ha, C., Tortorelli, D.: Stress-based topology optimization for continua. Structural and Multidisciplinary Optimization **41**(4), 605–620 (2010). https://doi.org/10.1007/s00158-009-0440-y

[33] Lee, K., Ahn, K., Yoo, J.: A novel P-norm correction method for lightweight topology optimization under maximum stress constraints. Computers & Structures **171**, 18–30 (2016). https://doi.org/10.1016/j.compstruc.2016.04.005

[34] Fan, Z., Xia, L., Lai, W., Xia, Q., Shi, T.: Evolutionary topology optimization of continuum structures with stress constraints. Structural and Multidisciplinary Optimization **59**(2), 647–658 (2019). https://doi.org/10.1007/s00158-018-2090-4

[35] Kennedy, G.J., Hicken, J.E.: Improved constraint-aggregation methods.

Computer Methods in Applied Mechanics and Engineering **289**, 332–354 (2015). https://doi.org/10.1016/j.cma.2015.02.017

[36] Norato, J.A., Smith, H.A., Deaton, J.D., Kolonay, R.M.: A maximum-rectifier-function approach to stress-constrained topology optimization. Structural and Multidisciplinary Optimization **65**, 286 (2022). https://doi.org/10.1007/s00158-022-03357-z

[37] da Silva, G.A., Beck, A.T., Sigmund, O.: Stress-constrained topology optimization considering uniform manufacturing uncertainties. Computer Methods in Applied Mechanics and Engineering **344**, 512–537 (2019). https://doi.org/10.1016/j.cma.2018.10.020

[38] da Silva, G.A., Beck, A.T., Sigmund, O.: Topology optimization of compliant mechanisms with stress constraints and manufacturing error robustness. Computer Methods in Applied Mechanics and Engineering **354**, 397–421 (2019). https://doi.org/10.1016/j.cma.2019.05.046

[39] Giraldo-Londoño, O., Paulino, G.H.: Polystress: a matlab implementation for local stress-constrained topology optimization using the augmented Lagrangian method. Structural and Multidisciplinary Optimization **63**(4), 2065–2097 (2021). https://doi.org/10.1007/s00158-020-02760-8

[40] Sherif, K., Witteveen, W., Puchner, K., Irschik, H.: Efficient topology optimization of large dynamic finite element systems using fatigue. AIAA Journal **48**(7), 1339–1347 (2010). https://doi.org/10.2514/1.45196

[41] Holmberg, E., Torstenfelt, B., Klarbring, A.: Fatigue constrained topology optimization. Structural and Multidisciplinary Optimization **50**(2), 207–219 (2014). https://doi.org/10.1007/s00158-014-1054-6

[42] Jeong, S.H., Choi, D.-H., Yoon, G.H.: Fatigue and static failure considerations using a topology optimization method. Applied Mathematical Modelling **39**(3), 1137–1162 (2015). https://doi.org/10.1016/j.apm.2014.07.020

[43] Collet, M., Bruggi, M., Duysinx, P.: Topology optimization for minimum weight with compliance and simplified nominal stress constraints for fatigue resistance. Structural and Multidisciplinary Optimization **55**(3), 839–855 (2017). https://doi.org/10.1007/s00158-016-1510-6

[44] Oest, J., Lund, E.: Topology optimization with finite-life fatigue constraints. Structural and Multidisciplinary Optimization **56**(5), 1045–1059 (2017). https://doi.org/10.1007/s00158-017-1701-9

[45] Chen, Z., Long, K., Wen, P., Nouman, S.: Fatigue-resistance topology optimization of continuum structure by penalizing the cumulative fatigue

damage. Advances in Engineering Software **150**, 102924 (2020). https://doi.org/10.1016/j.advengsoft.2020.102924

[46] James, K.A., Waisman, H.: Topology optimization of structures under variable loading using a damage superposition approach. International Journal for Numerical Methods in Engineering **101**, 375–406 (2015). https://doi.org/10.1002/nme.4810

[47] Zhang, S., Le, C., Gain, A., Norato, J.: Fatigue-based topology optimization with non-proportional loads. Computer Methods in Applied Mechanics and Engineering **345**, 805–825 (2018). https://doi.org/10.1016/j.cma.2018.11.015

[48] Suresh, S., Lindström, S.B., Thore, C.-J., Torstenfelt, B., Klarbring, A.: Topology optimization using a continuous-time high-cycle fatigue model. Structural and Multidisciplinary Optimization **61**, 1011–1025 (2020). https://doi.org/10.1007/s00158-019-02400-w

[49] Suresh, S., Lindström, S.B., Thore, C.-J., Klarbring, A.: Topology optimization for transversely isotropic materials with high-cycle fatigue as a constraint. Structural and Multidisciplinary Optimization **63**, 161–172 (2021). https://doi.org/10.1007/s00158-020-02677-2

[50] Yvonnet, J., Ryckelynck, D., Lorong, P., Chinesta, F.: A new extension of the natural element method for non-convex and discontinuous problems: the constrained natural element method (C-NEM). International Journal for Numerical Methods in Engineering **60**(8), 1451–1474 (2004). https://doi.org/10.1002/nme.1016

[51] Sibson, R.: A brief description of natural neighbor interpolation. Interpreting Multivariate Data, 21–36 (1981)

[52] Belikov, V.V., Semenov, A.Y.: Non-Sibsonian interpolation on arbitrary system of points in Euclidean space and adaptive isolines generation. Applied Numerical Mathematics **32**(4), 371–387 (2000). https://doi.org/10.1016/S0168-9274(99)00058-6

[53] Sukumar, N., Moran, B., Belytschko, T.: The natural element method in solid mechanics. International Journal for Numerical Methods in Engineering **43**(5), 839–887 (1998). https://doi.org/10.1002/(SICI)1097-0207(19981115)43:5⟨839::AID-NME423⟩3.0.CO;2-R

[54] Chen, J.-S., Wu, C.-T., Yoon, S., You, Y.: A stabilized conforming nodal integration for Galerkin mesh-free methods. International Journal for Numerical Methods in Engineering **50**(2), 435–466 (2001). https://doi.org/10.1002/1097-0207(20010120)50:2⟨435::AID-NME32⟩3.0.CO;2-A

[55] Zegard, T., Paulino, G.H.: Bridging topology optimization and additive manufacturing. Structural and Multidisciplinary Optimization **53**(1), 175–192 (2016). https://doi.org/10.1007/s00158-015-1274-4

[56] Guest, J.K., Prévost, J.H., Belytschko, T.: Achieving minimum length scale in topology optimization using nodal design variables and projection functions. International Journal for Numerical Methods in Engineering **61**(2), 238–254 (2004). https://doi.org/10.1002/nme.1064

[57] Wang, F., Lazarov, B.S., Sigmund, O.: On projection methods, convergence and robust formulations in topology optimization. Structural and Multidisciplinary Optimization **43**(6), 767–784 (2011). https://doi.org/10.1007/s00158-010-0602-y

[58] Crossland, B.: Effect of large hydrostatic pressures on the torsional fatigue strength of an alloy steel. International Conference on Fatigue of Metals: Proceedings, London, UK (1956)

[59] Bertsekas, D.P.: Constrained Optimization and Lagrange Multiplier Methods. Academic Press, Belmont, Massachusetts, United States. (1982). https://doi.org/10.1016/C2013-0-10366-2

[60] Senhora, F.V., Giraldo-Londoño, O., Menezes, I.F.M., Paulino, G.H.: Topology optimization with local stress constraints: a stress aggregation-free approach. Structural and Multidisciplinary Optimization **62**(4), 1639–1668 (2020). https://doi.org/10.1007/s00158-020-02573-9

[61] Mower, T.M., Long, M.J.: Mechanical behavior of additive manufactured, powder-bed laser-fused materials. Materials Science and Engineering: A **651**, 198–213 (2016). https://doi.org/10.1016/j.msea.2015.10.068

[62] Fatemi, A., Molaei, R., Sharifimehr, S., Shamsaei, N., Phan, N.: Torsional fatigue behavior of wrought and additive manufactured Ti-6Al-4V by powder bed fusion including surface finish effect. International Journal of Fatigue **99**, 187–201 (2017). https://doi.org/10.1016/j.ijfatigue.2017.03.002

[63] Pereira, J.T., Fancello, E.A., Barcellos, C.S.: Topology optimization of continuum structures with material failure constraints. Structural and Multidisciplinary Optimization **26**, 50–66 (2004). https://doi.org/10.1007/s00158-003-0301-z